Simultaneous multiband radio-frequency detection using high-orbital-angular-momentum states in a Rydberg-atom receiver

Gianluca Allinson,* Matthew J. Jamieson, Andrew R. Mackellar, Lucy Downes, C. Stuart Adams, and Kevin J. Weatherill
Department of Physics, Durham University, South Road, Durham DH1 3LE, United Kingdom

(Received 13 December 2023; accepted 22 April 2024; published 24 June 2024)

We demonstrate simultaneous detection of radio-frequency (rf) fields ranging from the very high-frequency (VHF) band (128 MHz) to terahertz frequencies (0.61 THz) using high-orbital-angular-momentum (ℓ) states in a caesium Rydberg-atom receiver. rf fields are applied concurrently to a series of atomic transitions, where the application of each field allows access to the next-highest ℓ state and the energy separations between states become progressively smaller, allowing access to a very wide range of radio frequencies. We show that the optical response of the system in the presence of the rf fields can be reproduced theoretically using a simple Lindblad-master-equation approach. Furthermore, we demonstrate experimentally that a series of amplitude-modulated tones can be detected simultaneously using a wide range of carrier frequencies. This demonstration opens the way for Rydberg receivers to access low-frequency rf bands at low principal quantum number and allows for communications across multiple bands simultaneously using a single optical receiver. Moreover, the experimental method presented allows for high-resolution spectroscopy of high-orbital-angular-momentum states in alkali-metal atoms.

DOI: 10.1103/PhysRevResearch.6.023317

I. INTRODUCTION

Rydberg atoms, i.e., atoms in which an electron has been promoted to a highly excited state with large principal quantum number n, are increasingly finding use in technological applications [1]. The polarizability of atoms, and the transition strength between neighboring electronic states, both increase with increasing n, making Rydberg atoms highly sensitive to both ac and dc electric fields. This sensitivity has been exploited to demonstrate atom-based radio-frequency (rf) electric field metrology [2], rf sensing [3], THz imaging [4,5], and rf communications [6]. Most Rydberg-atom-based rf sensors make use of electromagnetically induced transparency (EIT) [7], a coherent and nondestructive process that couples the properties of the Rydberg state to an optical transition from the atomic ground state, thereby allowing the perturbative effect of an incoming rf electric field on the Rydberg state to be mapped onto an optical probe field, which is detected using a photodetector [8,9]. This EIT technique effectively enables sensitive and SI-traceable measurements of rf electric fields to be extracted from an optical signal [10]. The last decade has seen an explosion of development in this research area, with Rydberg-atom receivers demonstrating high performance in the measurement of rf field properties, from precision amplitude [3], frequency [11], and phase [3,12] measurements to polarization [13], angle of arrival [14], and simultaneous detection of multiple frequencies [15,16].

One of the major strengths of a Rydberg-atom rf receiver, when compared to other rf technologies, is its potential to detect an enormous frequency range using a single device [17]. Indeed, Rydberg-atom receivers have demonstrated rf field detection at frequencies ranging from below 1 kHz [18] to above 1 THz [19]. In the low-frequency, or quasi-dc detection regime [8,17,20], Rydberg receivers can achieve continuous frequency coverage but with limited sensitivity, whereas in the higher-frequency ac detection regime, the use of resonant atomic transitions allows far greater sensitivity to be achieved [2,3] but only over a small range of frequencies around resonance. Furthermore, the resonant frequency of Rydberg-Rydberg transitions decreases with increasing n, meaning that states with very high n (>100) are typically required to access frequencies below 1 GHz in the sensitive ac regime. Gaining access to low frequencies using higher n states places demanding requirements on the laser power needed for experiments. Furthermore, measurements at very high n can be affected negatively by atom-atom interactions, ionization, and dc Stark shifts [7].

Consequently, recent work has focused on gaining access to lower-frequency bands via the use of higher-angular-momentum states. For example, a three-step laser excitation scheme [21] plus an rf field can allow access to $nF \rightarrow n'G$ ($\ell = 3 \rightarrow \ell = 4$) transitions which extend the range of resonant rf transitions to $\sim$1 GHz at more accessible principal quantum numbers ($n \approx 70$) [22]. Similarly, $nF \rightarrow n'G$ can be accessed using two laser fields plus two rf fields, and have been used for satellite radio detection at 2.3 GHz [23]. Other recent work has demonstrated the capability of simultaneous demodulation at multiple carrier frequencies spanning a

*gianluca.allinson@durham.ac.uk

wide frequency range (1.7–116 GHz) using $n\mathrm{D} \rightarrow \mathrm{n}'\mathrm{P}$ and $n\mathrm{F} \rightarrow \mathrm{n}'\mathrm{D}$ transitions, with $0 \leqslant |n - n'| \leqslant 4$ [15]. Also worth mentioning is a recent proposal for dc electric field sensing which uses spectroscopy of states up to $\ell = 6$ in Rb [24].

In this work we build upon these principles of using higher-angular-momentum states and simultaneous application of multiple rf frequencies and take it much further. We demonstrate that a Rydberg-atom ensemble is capable of simultaneously detecting multiple rf fields (seven in this case) over adjacently coupled higher-angular-momentum states. These fields can be used as a set of discrete carriers which range from the very-high-frequency (VHF) band (30–300 MHz) to the THz band (0.3–3 THz), ultimately spanning 12 octaves. At frequencies that our rf emitters allow, amplitude-modulated tones are transmitted and detected simultaneously by mapping the modulation to the optical probe. This is achieved by using two optical photons to reach a Rydberg state and a sequence of cascading rf fields that resonantly couple higher-angular-momentum states in the atom. Furthermore, we demonstrate that the VHF range can be accessed at significantly lower principal quantum numbers, $n = 17$, where interatomic interactions and dc Stark effects are small and laser power requirements are lower.

By utilizing resonant transitions at significantly lower-frequency radio bands, we extend resonant ac Rydberg rf sensing to frequencies around 10^8 Hz, a frequency range where previous Rydberg receiver demonstrations have relied on nonresonant/quasi-dc methods that have far lower sensitivities than passive dipole electronic sensors [17].

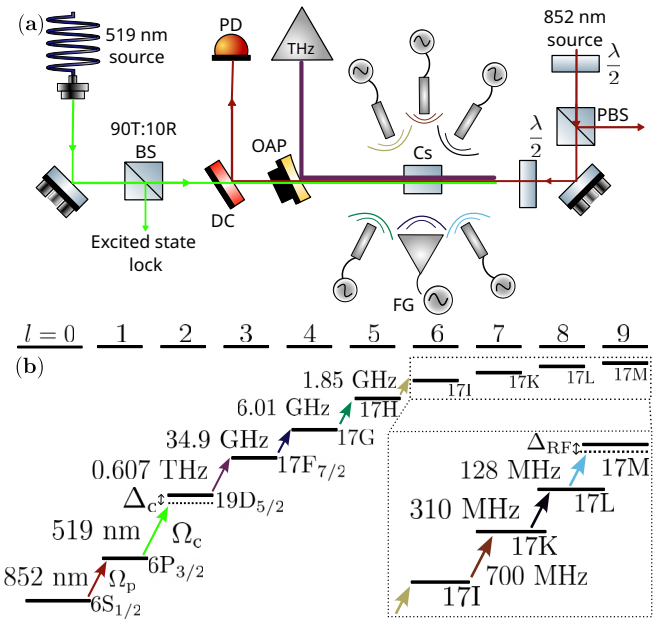

FIG. 1. (a) Experimental layout of the Rydberg receiver with 852-nm probe, 519-nm coupling, and 0.607-THz fields overlapping within the Cs vapor cell. DC - dichroic mirror, OAP - off-axis parabolic mirror, (P)BS, (polarizing) beam-splitter, FG - frequency generator, PD - photodiode, $\lambda/2$ - half-wave plate. A pyramidal rf gain horn and five whip antennas provide the rf fields. (b) An energy-level diagram showing the electronic states used. A zoomed inset shows the 17ℓ states with $\ell \geqslant 6$ for clarity. Transitions are color coded in (a) to their counterpart in (b) and subsequent figures.

II. METHOD

Simultaneous multiband rf field detection is implemented using laser spectroscopy of an atomic vapor. A schematic diagram of the experimental arrangement is shown in Fig. 1(a). A linearly polarized continuous wave (cw) 852-nm probe beam (solid red line), resonant with the $6S_{1/2}, F = 4 \rightarrow 6P_{3/2}, F' = 5$ transition, was passed through a 1-cm-long cuboidal cuvette containing caesium (Cs) vapor at room temperature (23 °C), with a number density estimated to be $\simeq 5 \times 10^{10}$ cm^{-3}, and then detected using a photodiode (PD). A counterpropagating and linearly polarized cw 519-nm coupling laser (solid green line) with detuning Δ_c from the $6P_{3/2} \rightarrow 19D_{5/2}$ transition was overlapped with the probe field using a dichroic mirror (DC). The probe and coupling beams have powers of 20 μW and 21 mW and $1/e^2$ beam waists of 1.20(7) mm and 0.96(7) mm, respectively. The probe beam is derived from a *Toptica DL pro* laser and stabilized using polarization spectroscopy [25]. The coupling beam is derived from a home-built second-harmonic generation system of a 1030-nm ECDL based on the design of Legaie *et al.* [26]. Cavity power buildup is stabilized by a modified Hänsch-Couillaud lock [27,28]. The coupling laser is frequency stabilized by an excited-state lock using nonlinear polarization spectroscopy [29]. A linearly polarized terahertz (THz) beam (solid purple line) resonant with the $19D_{5/2} \rightarrow 17F_{7/2}$ transition at 0.607 THz is launched from a diagonal horn antenna, collimated using a polytetrafluoroethylene (PTFE) lens (not shown) and focused in the Cs cell using an off-axis parabolic (OAP) mirror. The OAP contains a 2-mm through-hole to allow the laser beams to copropagate with the THz beam. The THz beam is derived from a *Virginia Diodes* amplifier multiplier chain (AMC) and is estimated to have a power of 10 μW and beam waist of approximately 1.5 mm within the cell. The transmission of the probe beam is recorded as the frequency of the coupling beam (Δ_c) is varied. The EIT spectrum obtained in the presence of the THz field is presented in Fig. 2(a). The rf fields are generated using frequency generators and emitted via commercial Wi-Fi, cellular, and radio $\lambda/4$ monopole whip antennas that are placed approximately 10–20 cm from the cell where there is clear line-of-sight. The inclusion of each additional field changes the transmission profile of the probe beam as shown in Figs. 2(b)–2(g). The transitions used are shown schematically in Fig. 1(b), with their frequencies and numerically calculated dipole matrix elements (DMEs) presented in Table I [30]. We exploit the fact that beyond $\ell \geqslant 3$, transitions of the form $n\ell \rightarrow n(\ell + 1)$ allow for lower-frequency bands to be addressed. The rapidly decreasing overlap of the electron wave function with the atomic core results in extremely small quantum defects, and hence small energy separations, of high-ℓ states [31]. Each rf field is applied such that it is resonant with the transition to the next-highest-angular-momentum atomic state. A higher ℓ state can only be coupled if the lower ℓ state is coupled by the relevant rf field. Consequently, the $17L \rightarrow 17\mathrm{M}$ coupling at 128 MHz is dependent on all previous states to be coupled by their resonant rf and optical fields. When the high-ℓ states are all simultaneously coupled by their respective resonant

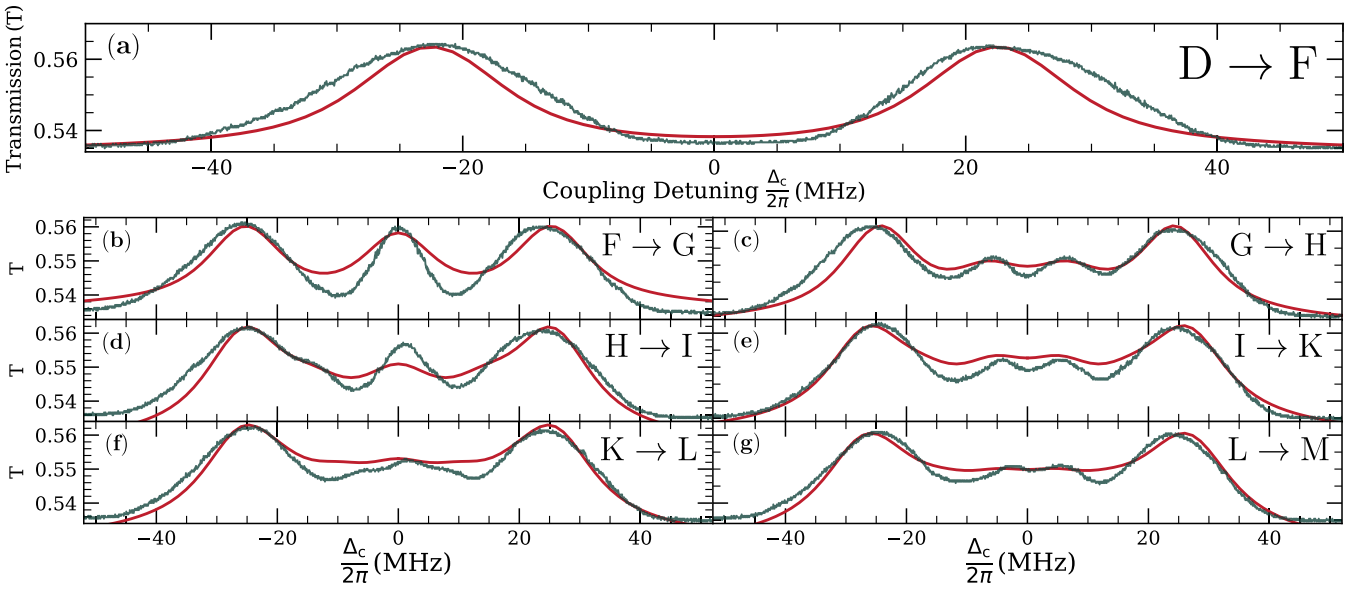

FIG. 2. Absolute probe transmission traces from the experiment (green) with each subsequent addition of a field in the ladder system overlaid with an n-level master equation model (red). The frequency scale is calibrated via the $6P_{3/2}$ $F = 4$, $F = 5$ separation. (a) The probe and coupling field with the THz field resonant to the $19D_{5/2} \rightarrow 17F_{7/2}$ transition. The subsequent microwave fields are then resonant with the (b) $17F_{7/2} \rightarrow 17G$, (c) $17G \rightarrow 17H$, (d) $17H \rightarrow 17I$, (e) $17I \rightarrow 17K$, (f) $17K \rightarrow 17L$, and (g) and $17L \rightarrow 17M$ transitions. Each transition is labeled with the respective $\ell \rightarrow \ell'$ for clarity.

rf fields, we amplitude modulate five of the seven fields and detect the baseband tones on the optical signal. For all data, readout is taken from the photodiode via USB-DAQ of an oscilloscope and no lock-in detection/amplification is used.

III. RESULTS

A. Multilevel EIT cascade scheme

The experimental spectra in Fig. 2 can be understood in terms of a N-level EIT cascade scheme [32]. With the probe laser locked, a transparency window in the probe absorption profile is expected at around $\Delta_c = 0$, resulting in a coherent transmission feature as the coupling laser is detuned across this resonance. This phenomenon is known as electromagnetically induced transparency (EIT) [7]. Applying the THz field results in a reduction in transmission of the probe field at $\Delta_c = 0$. For large THz field strengths, this results in the Autler-Townes (AT) splitting seen prominently in Fig. 2(a). With the addition of another field, there is again transparency in the line center. This is apparent in the data in the left-hand column of Fig. 2, showing a distinct increase in the probe transmission at zero detuning of the coupling field for an odd number of levels. For an even number of levels, there is absorption about the line center, shown in the right-hand column of Fig. 2. When the subsequent rf fields are applied, the previous resultant AT splitting is further shifted from the line center and decreases in amplitude. These features become hard to distinguish in the line shape; nevertheless, modulation of these fields causes a change to the transmission of the probe beam. The atomic ensemble is modeled using a Lindblad-master-equation approach, which gives a time evolution of the density matrix, $\hat{\rho}$:

$$\frac{d\hat{\rho}}{dt} = -\frac{i}{\hbar}[\hat{H}, \hat{\rho}] + \hat{L}_{\text{atom}} + \hat{L}_{\text{dephasing}}, \tag{1}$$

where $\hat{H}$ is the Hamiltonian of the atom-light system, $\hat{L}_{\text{atom}}$ is the Lindblad superoperator describing spontaneous decay, and $\hat{L}_{\text{dephasing}}$ is dephasing due to the laser linewidths or collisional effects. The series of differential equations formed are then solved in the steady state to give the susceptibility of the atomic ensemble [33]. The system is repeatedly solved for varying velocity classes and integrated over a bounded velocity distribution to obtain the Doppler-broadened profile. Outside the weak probe regime, numerical solutions are needed. Minimization of numerical solutions inclusive of Doppler broadening is computationally expensive. Instead, model inputs such as the Rabi frequencies for each field were

TABLE I. A list of the electronic states that are coupled by the series of cascading rf fields. DME - (Radial) dipole matrix element. While the fine structure splitting is not resolved beyond F, we label the strongest coupled j state for completeness. Note that by convention "J" is omitted as the symbol for the $\ell = 7$ azimuthal quantum number.

Atomic transition	Final ℓ	rf (GHz)	DME (ea_0)
$19D_{5/2} \rightarrow 17F_{7/2}$	3	607	354
$17F_{7/2} \rightarrow 17G_{9/2}$	4	34.9	423
$17G_{9/2} \rightarrow 17H_{11/2}$	5	6.01	414
$17H_{11/2} \rightarrow 17I_{13/2}$	6	1.85	406
$17I_{13/2} \rightarrow 17K_{15/2}$	7	0.700	395
$17K_{15/2} \rightarrow 17L_{17/2}$	8	0.310	383
$17L_{17/2} \rightarrow 17M_{19/2}$	9	0.128	368

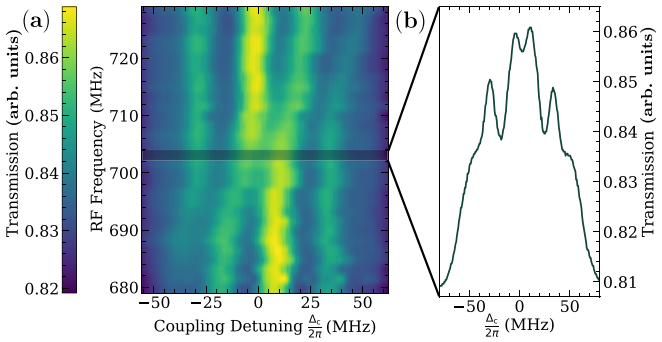

FIG. 3. Spectral map of the $I \rightarrow K$ transition as the rf field is swept and coupling laser is detuned across resonance. (a) A color map made up of the resultant probe transmission traces in response to scanning the rf field over resonance for the $17I \rightarrow 17K$ transition at ∼700 MHz. (b) A plot of the probe transmission vs the coupling detuning for an rf field of 0.703 GHz, a gray bar shows the EIT trace that makes up that respective part of the color map.

varied around the experimental values to give the best fit by eye.

The resulting model spectra are shown by the red lines in Fig. 2, along with those from the experiment. Only one m_j state is used for each level; including all sublevels would result in a model consisting of 110 levels. Fine structure beyond the F state is ignored, but note that the $j = \ell + \frac{1}{2}$ states are most strongly coupled, and transitions to these states are assumed in the calculation of dipole matrix elements for G, H, and beyond. We find good agreement with the model in the generality of adding additional levels. The parameters used for the model were $\Omega_p = 2\pi \times 1.8$ MHz, $\Omega_c = 2\pi \times 3.7$ MHz, and $\Omega_{THz} = 2\pi \times 46$ MHz. The remaining Rabi frequencies of the rf fields varied by a few MHz but were approximately $2\pi \times 20$ MHz. Increasing the power of the THz field, which is limited due to technical restraints, would result in a larger transmission window and hence better estimation of the Rabi frequencies of subsequent fields without the use of a model. Each distinct splitting could be distinguished and measured directly from the experimental data.

Figure 3(a) shows behavior of the lines shape in response to detuning the rf field from resonance. Here the probe laser power (∼100 μW) and the power of the rf fields are increased in order to improve signal to noise and visibility of the distinct AT splittings arising from each of the rf field couplings. The contrast is seen in Fig. 3(b) when compared to Fig. 2(e), whereby each of the distinct AT peaks are separated and can be distinguished.

The transmission window in the line shape persists over a large detuning range, $\Delta_{rf} = \pm 20$ MHz. As this is an even level system, the induced transparency from the presence of the previous field slowly shifts about the line center and splits until symmetric at $\Delta_{rf} = 0$ MHz. The resonance of the feature is seen at ∼705 MHz compared to the previously observed 700 MHz used in Fig. 2(e). This can be attributed to ac Stark shifts or detunings of previous fields that accumulate error for each rf field that is on resonance.

B. Amplitude modulation of resonant rf fields

The rf fields were modulated to demonstrate simultaneous detection across the various frequencies that are resonant with the atomic transitions. A change in each rf field amplitude will independently change the transmission of the probe beam. When amplitude modulated, the baseband tones on each rf field can then be extracted via performing a fast Fourier transform (FFT) of the probe transmission signal. In a Rydberg-atom detector, demodulation of the rf frequencies are performed by the atom in and of itself, so no additional demodulation of the signal is necessary.

Each of the electronic states detailed above were simultaneously coupled by the probe, coupling, THz, and the six rf fields with powers similar to those used in the spectra of Fig. 3. A baseband tone in the kHz frequency range was modulated on each carrier rf field and detailed in Fig. 4. The modulation

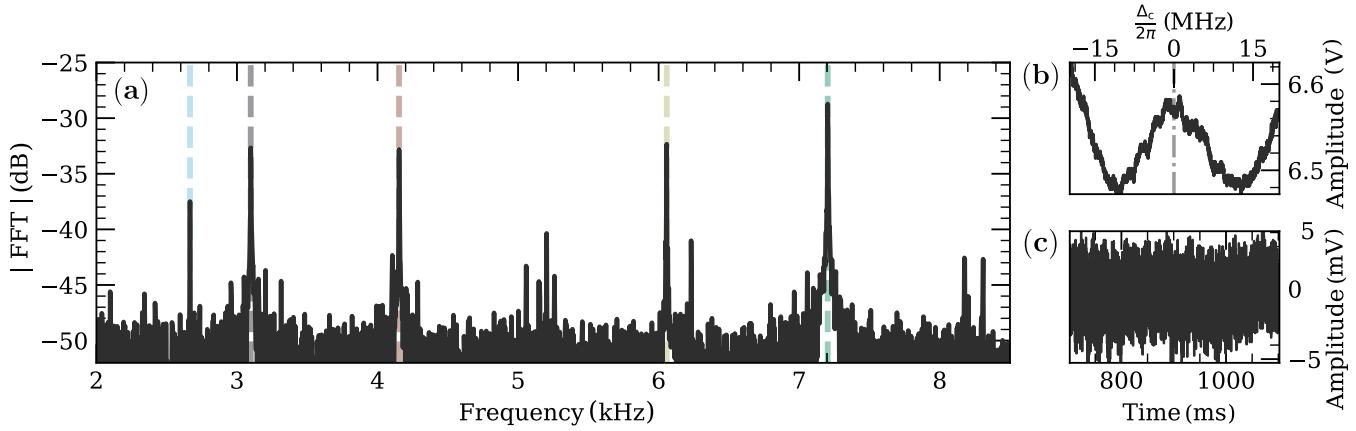

FIG. 4. Simultaneous detection of five independent AM tones using five of the seven rf carriers. (a) The modulus of an FFT of the probe transmission at $\Delta_c = 0$. The amplitude-modulated tones used were 7.2 kHz, 6.05 kHz, 4.15 kHz, 3.1 kHz, and 2.66 kHz on carrier frequencies of 6.01 GHz, 1.85 GHz, 700 MHz, 310 MHz, and 128 MHz, respectively. A dashed line is shown on each of the peaks for visual aid. The resolution bandwidth is 2.5 Hz. (b) An inset showing a typical scan of an EIT feature during modulation of the rf fields. A vertical dashed line shows the point at which the coupling laser is locked. (c) A typical trace before it is discrete Fourier transformed.

index of the AM used on all of the carrier frequencies was 0.5. The resulting modulus of the fast Fourier transform of the probe signal is shown in Fig. 4(a).

The data show that the baseband tone from each of the independent carriers can be recovered from the probe signal. The decreasing strength of the FFT signal as the carrier frequency decreases can be partially attributed to the decreasing DME of the transitions. In order to remove servo noise that we observed in the FFT, the data presented is taken by disengaging the coupling laser frequency lock and subsequently saving a trace. Due to technical limitations, the THz source and a 34.9-GHz megawatt generator could not be amplitude modulated. However, there is nothing to suggest that amplitude modulation of these transitions could not be detected.

IV. DISCUSSION

In principle, the number of fields that could be applied is limited by the possible angular momentum states, $(n-1)$. At higher principal quantum number, the sensitivity to the fields would increase and the splitting between neighboring ℓ states would decrease. For example, neighboring angular momentum transitions $\ell \geqslant 8$ at higher n (40–70) would correspond to resonant fields in the medium-frequency (300 kHz–3 MHz) or high-frequency (3 MHz–30 MHz) radio bands.

We note that at low n, many perturbing effects such as dc-Stark-induced state mixing and Rydberg-Rydberg collisions are significantly reduced [31]. Despite the lower sensitivity to external rf fields, electrometry at low principal quantum number may be more suitable for calibration of an rf field or metrology applications.

In this work Rabi frequencies were chosen so that transition frequencies could be determined from visual inspections of the line shape. Consequently, the rf field strengths detected throughout this manuscript are large and approximately $\simeq$9 V/m, although this is not in the limit of a minimum detectable field.

A sensitivity assessment of the method to each of the applied rf fields is beyond the scope of this paper, as the sensitivity for each transition depends upon the driving strength of all previous transitions, making the parameter space very large. Regardless, we note that our sensitivity could be improved using rf heterodyning techniques and lock-in detection. Heating the cell would also improve signal-to-noise ratio by increasing number density. Furthermore, the use of other well-characterized antennas for the lower-frequency fields would allow a better estimation of the electric field strengths involved. The $\lambda/4$ monopole antennas used are not well characterized, are omnidirectional, and have poor efficiency, resulting in significant power loss before the cell.

The method presented above could be used to investigate higher-angular-momentum states in alkali metals, which are not as well studied as the S, P, D, and F states. There is currently no published work on quantum defects in Cs higher than $G_{7/2}$ known to the authors [34,35], while some exists for rubidium [36–38]. Transitions were found in this work by sweeping the frequency of the rf fields to observe the largest change in transmission of the probe beam at low rf power. Initial estimations of the transition frequencies were given by `ARC`, an open-source library for calculating properties of alkali Rydberg atoms, which uses an approximation to calculate the various higher ℓ quantum defects, $\delta_{\ell,j}$, for $\ell \geqslant 4$ based on the measured Cs $G_{7/2}$ quantum defect [39]. The observed resonances were found to be in general agreement and were additionally compared to the scarce available literature [40]. Discrepancies on the order of several MHz are found for $\ell \geqslant 5$ in comparison to said literature. There is no control of stray magnetic-electric fields, which may cause further splitting of the numerous m_J states. Additional discussion of using the experimental method presented for precision spectroscopy of high-ℓ states is presented, along with associated systematic error, in the Appendix.

V. CONCLUSION

Simultaneous detection of rf fields across 12 octaves by an optically coherent method is demonstrated. The method opens a way of conducting radio-frequency electrometry using a cascade of rf fields across adjacent angular momentum coupled states. We have furthermore demonstrated that the simultaneous amplitude modulation of several of these rf fields can be clearly resolved in the resulting EIT optical signal, offering a path to simultaneous multiband rf communication at increasingly lower radio bands using significantly lower principal quantum numbers. Further work should be done to characterize and optimize the technique both for higher principal quantum number and three-photon electrometry methods.

The data presented in this paper are available [41].

ACKNOWLEDGMENTS

The authors would like to thank Robert Potvliege and Popoola Waisu for useful discussions, Ifan Hughes for careful reading of the manuscript, Jonathan Pritchard for SHG laser designs, and Mike Tarbutt for the loan of equipment. We acknowledge the UK Engineering and Physical Sciences Research Council under Grants No. EP/R002061/1, No. EP/V030280/1, No. EP/W009404/1, and No. EP/W033054/1.

APPENDIX: DETERMINING TRANSITION FREQUENCIES USING EIT IN LADDER SYSTEMS

In the ladder excitation scheme, addition of an rf field resonant with an adjacent level modifies the spectrum in one of

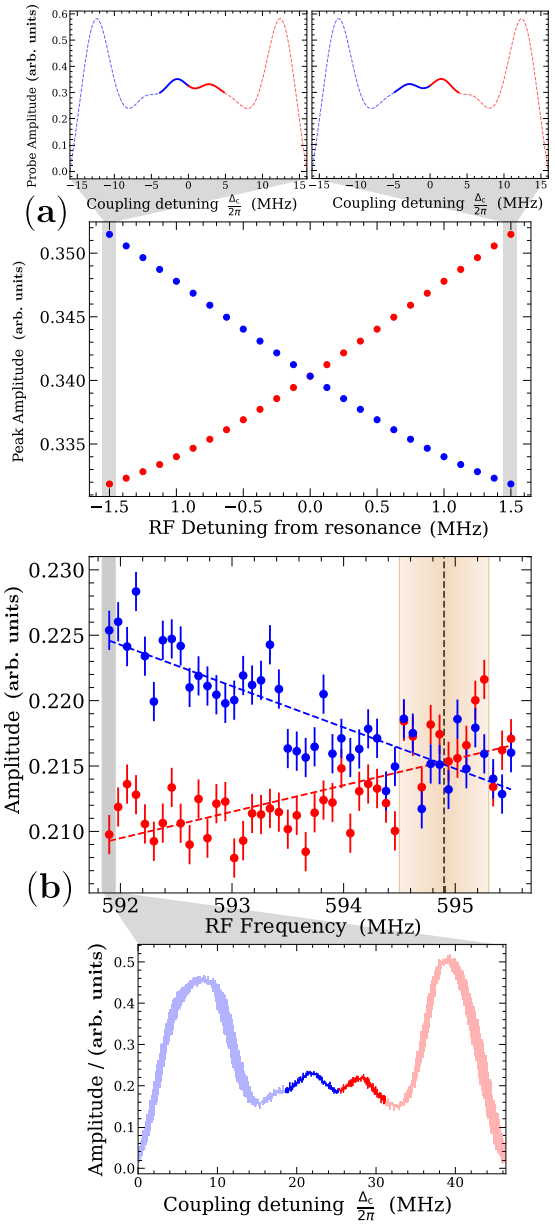

FIG. 5. Demonstration of method for determining transition frequencies using EIT in ladder systems. (a) Modeled peak amplitudes (using [33]) against rf detuning, extracted from AT splittings of the $18I \rightarrow 18K$ transition. The two insets show modeled spectra when the rf field is detuned 1.5 MHz either side of the $18I \rightarrow 18K$ resonance, corresponding to the first and last pairs of data points. (b) Measured peak amplitude data of the $18I \rightarrow 18K$ transition as the rf is detuned. The straight dashed line fit determines where the AT splittings have the same amplitude, assumed to be on resonance when neglecting perturbing effects. The blacked dashed line shows the extracted transition frequency, 594.9(4) MHz, and the error as the shaded beige band, calculated from statistics of the fit. The inset shows the measured spectrum used to extract the first pair of data points when the rf field is 592 MHz.

two ways. For even numbers of levels, a strong rf field causes an Autler-Townes (AT) splitting in the line shape, resulting in two distinct peaks appearing in the spectrum. On resonance, the amplitudes of these peaks are equal, which can be used as criteria for determining the exact transition frequency. For small detuning about resonance, the change in amplitude of the features is linear [42], and the transition frequency can be extracted from the intersection of two straight-line fits as shown in Fig. 5. The main source of error from statistical fits is derived from the laser amplitude noise, which causes a change in probe transmission. This could be reduced in experiment via use of laser amplitude stabilizers and by an increase of coupling power to increase the signal-to-noise ratio.

Any detuning from resonance of the previous fields in the ladder scheme will cause an asymmetry in the line shape. This compounds into a change in the measured resonant frequency of subsequent fields by shifting the AT peak amplitudes. We minimized this uncertainty by first measuring transition frequencies of previous resonant fields before those of subsequent fields. The uncertainty in these measurements can then be taken as the uncertainty in the rf detuning of the following field.

The dc Stark effect results in a shift of the transition frequency due to stray electric fields in the cell, introducing a further uncertainty. It has been recently highlighted that the polarizability scales significantly with high-ℓ states and as such would present a significant uncertainty on the higher ℓ transitions measured [24]. While we cannot currently reliably measure the magnitude of any stray dc electric fields in the cell, we can place bounds on the expected shift using the polarizability of the state of interest. For example, the polarizability of the $n = 17I$ ($\ell = 6$) state is 119 MHz cm^{-2}/V^2 [30]. From this we can calculate that a dc electric field uncertainty of order 0.1 V/cm results in a 0.6-MHz error in the measured transition frequency. At higher principal quantum number, this effect presents a significant uncertainty due to the already present n^7 scaling. The 40I state has an expected polarizability of (56.8×10^3) MHz cm^{-2}/V^2.

The ac Stark effect may become significant as the number of fields increase during higher ℓ measurements. Again, this can be minimized by first taking a measurement of the dressing field at low power to minimize this shift. Numerical models, such as `ARC`, could be used to estimate the ac Stark shift for a given electric field strength that could be estimated from the Rabi frequency of said field. The shift in the resonance of subsequent fields could be investigated against the field strength of previous fields, and the resonant frequency could be taken in the limit of zero field strength.

[1] C. S. Adams, J. D. Pritchard, and J. P. Shaffer, Rydberg atom quantum technologies, J. Phys. B: At. Mol. Opt. Phys. **53**, 012002 (2019).

[2] J. A. Sedlacek, A. Schwettmann, H. Kuebler, R. Loew, T. Pfau, and J. P. Shaffer, Microwave electrometry with Rydberg atoms in a vapour cell using bright atomic resonances, Nat. Phys. **8**, 819 (2012).

[3] M. Jing, Y. Hu, J. Ma, H. Zhang, L. Zhang, L. Xiao, and S. Jia, Atomic superheterodyne receiver based on microwave-dressed Rydberg spectroscopy, Nat. Phys. **16**, 911 (2020).

[4] C. G. Wade, N. Šibalić, N. R. de Melo, J. M. Kondo, C. S. Adams, and K. J. Weatherill, Real-time near-field terahertz imaging with atomic optical fluorescence, Nat. Photonics **11**, 40 (2017).

[5] L. A. Downes, A. R. MacKellar, D. J. Whiting, C. Bourgenot, C. S. Adams, and K. J. Weatherill, Full-field terahertz imaging at kilohertz frame rates using atomic vapor, Phys. Rev. X **10**, 011027 (2020).

[6] Z. Song, H. Liu, X. Liu, W. Zhang, H. Zou, J. Zhang, and J. Qu, Rydberg-atom-based digital communication using a continuously tunable radio-frequency carrier, Opt. Express **27**, 8848 (2019).

[7] A. K. Mohapatra, T. R. Jackson, and C. S. Adams, Coherent optical detection of highly excited Rydberg states using electromagnetically induced transparency, Phys. Rev. Lett. **98**, 113003 (2007).

[8] A. K. Mohapatra, M. G. Bason, B. Butscher, K. J. Weatherill, and C. S. Adams, A giant electro-optic effect using polarizable dark states, Nat. Phys. **4**, 890 (2008).

[9] M. Tanasittikosol, J. D. Pritchard, D. Maxwell, A. Gauguet, K. J. Weatherill, R. M. Potvliege, and C. S. Adams, Microwave dressing of Rydberg dark states, J. Phys. B: At., Mol. Opt. Phys. **44**, 184020 (2011).

[10] H. Fan, S. Kumar, J. Sedlacek, H. Kübler, S. Karimkashi, and J. P. Shaffer, Atom based rf electric field sensing, J. Phys. B: At., Mol. Opt. Phys. **48**, 202001 (2015).

[11] J. A. Gordon, M. T. Simons, A. H. Haddab, and C. L. Holloway, Weak electric-field detection with sub-1 Hz resolution at radio frequencies using a Rydberg atom-based mixer, AIP Adv. **9**, 045030 (2019).

[12] M. T. Simons, A. H. Haddab, J. A. Gordon, and C. L. Holloway, A Rydberg atom-based mixer: Measuring the phase of a radio frequency wave, Appl. Phys. Lett. **114**, 114101 (2019).

[13] J. A. Sedlacek, A. Schwettmann, H. Kubler, and J. P. Shaffer, Atom-based vector microwave electrometry using rubidium Rydberg atoms in a vapor cell, Phys. Rev. Lett. **111**, 063001 (2013).

[14] A. K. Robinson, N. Prajapati, D. Senic, M. T. Simons, and C. L. Holloway, Determining the angle-of-arrival of a radio-frequency source with a Rydberg atom-based sensor, Appl. Phys. Lett. **118**, 114001 (2021).

[15] D. H. Meyer, J. C. Hill, P. D. Kunz, and K. C. Cox, Simultaneous multiband demodulation using a Rydberg atomic sensor, Phys. Rev. Appl. **19**, 014025 (2023).

[16] M. Jayaseelan, A. P. Rotunno, N. Prajapati, S. Berweger, A. B. Artusio-Glimpse, M. T. Simons, and C. L. Holloway, Electromagnetically-induced-transparency spectra of Rydberg atoms dressed with dual-tone radio-frequency fields, Phys. Rev. A **108**, 033712 (2023).

[17] D. H. Meyer, Z. A. Castillo, K. C. Cox, and P. D. Kunz, Assessment of Rydberg atoms for wideband electric field sensing, J. Phys. B: At., Mol. Opt. Phys. **53**, 034001 (2020).

[18] Y.-Y. Jau and C. Tony, Vapor-cell-based atomic electrometry for detection frequencies below 1 kHz, Phys. Rev. Appl. **13**, 054034 (2020).

[19] S. Chen, D. J. Reed, A. R. MacKellar, L. A. Downes, N. F. A. Almuhawish, M. J. Jamieson, C. S. Adams, and K. J. Weatherill, Terahertz electrometry via infrared spectroscopy of atomic vapor, Optica **9**, 485 (2022).

[20] D. H. Meyer, P. D. Kunz, and K. C. Cox, Waveguide-coupled Rydberg spectrum analyzer from 0 to 20 GHz, Phys. Rev. Appl. **15**, 014053 (2021).

[21] C. Carr, M. Tanasittikosol, A. Sargsyan, D. Sarkisyan, C. S. Adams, and K. J. Weatherill, Three-photon electromagnetically induced transparency using Rydberg states, Opt. Lett. **37**, 3858 (2012).

[22] R. C. Brown, B. Kayim, M. A. Viray, A. R. Perry, B. C. Sawyer, and R. Wyllie, Very-high-and ultrahigh-frequency electric-field detection using high angular momentum Rydberg states, Phys. Rev. A **107**, 052605 (2023).

[23] P. K. Elgee, J. C. Hill, K.-J. E. LeBlanc, G. D. Ko, P. D. Kunz, D. H. Meyer, and K. C. Cox, Satellite radio detection via dual-microwave Rydberg spectroscopy, Appl. Phys. Lett. **123**, 084001 (2023).

[24] A. Duspayev, R. Cardman, D. A. Anderson, and G. Raithel, High-angular-momentum Rydberg states in a room-temperature vapor cell for dc electric-field sensing, Phys. Rev. Res. **6**, 023138 (2024).

[25] C. Pearman, C. Adams, S. Cox, P. Griffin, D. Smith, and I. Hughes, Polarization spectroscopy of a closed atomic transition: Applications to laser frequency locking, J. Phys. B: At., Mol. Opt. Phys. **35**, 5141 (2002).

[26] R. Legaie, C. J. Picken, and J. D. Pritchard, Sub-kilohertz excitation lasers for quantum information processing with Rydberg atoms, J. Opt. Soc. Am. B **35**, 892 (2018).

[27] T. Hansch and B. Couillaud, Laser frequency stabilization by polarization spectroscopy of a reflecting reference cavity, Opt. Commun. **35**, 441 (1980).

[28] M. Vainio, J. Bernard, and L. Marmet, Cavity-enhanced optical frequency doubler based on transmission-mode Hänsch–Couillaud locking, Appl. Phys. B **104**, 897 (2011).

[29] D. H. Meyer, P. D. Kunz, and N. Solmeyer, Nonlinear polarization spectroscopy of a Rydberg state for laser stabilization, Appl. Opt. **56**, B92 (2017).

[30] N. Šibalić, J. D. Pritchard, C. S. Adams, and K. J. Weatherill, Arc: An open-source library for calculating properties of alkali Rydberg atoms, Comput. Phys. Commun. **220**, 319 (2017).

[31] T. F. Gallagher, Rydberg atoms, in *Springer Handbook of Atomic, Molecular, and Optical Physics* (Springer, New York, 1994), pp. 231–240.

[32] D. McGloin, D. Fulton, and M. Dunn, Electromagnetically induced transparency in n-level cascade schemes, Opt. Commun. **190**, 221 (2001).

[33] L. Downes, Simple Python tools for modelling few-level atom-light interactions, J. Phys. B: At., Mol. Opt. Phys. **56**, 223001 (2023).

[34] K.-H. Weber and C. J. Sansonetti, Accurate energies of *nS*, *nP*, *nD*, *nF*, and *nG* levels of neutral cesium, Phys. Rev. A **35**, 4650 (1987).

[35] C. J. Lorenzen and K. Niemax, Precise quantum defects of nS, nP and nD levels in Cs I, Z. Phys. A **315**, 127 (1984).

[36] S. Civiš, M. Ferus, P. Kubelík, V. E. Chernov, and E. M. Zanozina, Fourier transform infrared emission spectra of atomic rubidium: g- and h-states, J. Phys. B: At., Mol. Opt. Phys. **45**, 175002 (2012).

[37] S. J. Berl, C. A. Sackett, T. F. Gallagher, and J. Nunkaew, Core polarizability of rubidium using spectroscopy of the *ng* to *nh*, *ni* Rydberg transitions, Phys. Rev. A **102**, 062818 (2020).

[38] K. Moore, A. Duspayev, R. Cardman, and G. Raithel, Measurement of the Rb *g*-series quantum defect using two-photon microwave spectroscopy, Phys. Rev. A **102**, 062817 (2020).

[39] E. J. Robertson, N. Šibalić, R. M. Potvliege, and M. P. Jones, Arc 3.0: An expanded Python toolbox for atomic physics calculations, Comput. Phys. Commun. **261**, 107814 (2021).

[40] K. A. Safinya, T. F. Gallagher, and W. Sandner, Resonance measurements of f-h and f-i intervals in cesium using selective and delayed field ionization, Phys. Rev. A **22**, 2672 (1980).

[41] G. Allinson, M. J. Jamieson, A. R. Mackellar, L. Downes, C. S. Adams, and K. J. Weatherill, Data for "Simultaneous multi-band radio-frequency detection using high-orbital-angular-momentum states in a Rydberg-atom receiver," https://doi.org/10.15128/r12f75r8059.

[42] L. Downes, A high-speed THz imaging system based on THz-to-optical conversion in atomic vapour, Ph.D. thesis, Durham University, 2020.